

Demonstration of Efficient Radon Removal by Silver-Zeolite in a Dark Matter Detector

Daniel Durnford ^{1,*} Yuqi Deng ^{1,†} Carter Garrah^{1,‡} Philippe Gros,² Michel Gros,³ José Busto,⁴ Steven Kuznicki,⁵ and Marie-Cécile Piro ^{1,§}

¹*Department of Physics, University of Alberta, Edmonton, AB, T6G 2E1, Canada*

²*Department of Physics, Engineering Physics, and Astronomy,
Queen's University, Kingston, Ontario K7L 3N6, Canada*

³*IRFU, CEA, Université Paris-Saclay, F-91191 Gif-sur-Yvette, France*

⁴*Aix-Marseille Université, CNRS/IN2P3, CPPM, Marseille, 13288, France*

⁵*Department of Chemical and Materials Engineering,
University of Alberta, Edmonton, AB T6G 2R3, Canada*

We present the performance of an efficient radon trap using silver-zeolite Ag-ETS-10, measured with a spherical proportional counter filled with an argon/methane mixture. Our study compares the radon reduction capabilities of silver-zeolite and the widely used activated charcoal, both at room temperature. We demonstrate that silver-zeolite significantly outperforms activated charcoal by three orders of magnitude in radon capture. Given that radon is a major background contaminant in rare event searches, our findings highlight silver-zeolite as a highly promising adsorbent, offering compelling operational advantages for both current and future dark matter and neutrino physics experiments. Additionally, this holds great promise for developing future radon reduction systems in underground laboratories in order to increase their supporting capabilities for ton-scale experiments.

Radon (^{222}Rn), a naturally occurring radioactive noble gas produced from the decay of ^{238}U , poses significant challenges to low-background detection techniques in particle physics. As a major contaminant, radon compromises the sensitivity of experiments such as dark matter searches and neutrino physics studies [1–39]. ^{222}Rn decays by emitting an alpha particle with an energy of 5.49 MeV and has a half-life of 3.82 days [40]. Its decay chain includes two other alpha emitters, ^{218}Po and ^{214}Po , before finally producing ^{210}Pb , which is also a significant background source [19, 31, 41–44]. As a noble gas, radon can continuously emanate from the detector material and other components such as gas filters and pumps, and subsequently diffuse through the active target. Beta emitters from the ^{222}Rn decay chain, such as ^{214}Pb and ^{210}Pb , can also contribute to a homogeneous background of low-energy events in the region of interest for rare event searches that cannot be discriminated against in data analysis [41–43, 45]. Although existing cryogenic methods—such as activated charcoal or copper traps [1, 16, 46–50] and distillation [35, 45, 51]—have shown good radon removal performance, the increasing complexity and expansion to ton-scale experimental setups [18, 37, 38, 52–66] require the development of more efficient and practically optimized removal techniques.

This Letter presents a radon trap system developed for the New Experiments with Spheres-Gas (NEWS-G) dark matter experiment, currently achieving world-leading dark matter sensitivity [67, 68]. The detector consists of a spherical proportional counter (SPC) filled with a noble gas mixture. It is equipped with a high-voltage (HV) sensor in the middle to achieve high avalanche amplification gain while having a linear energy response and low electronic noise [69, 70]. As a

gaseous ionization detector, an SPC is capable of observing the energy response of single electrons [71], which makes it an ideal detector for searching for sub-GeV/ c^2 dark matter candidates. However, electronegative impurities in the gas—such as water and oxygen—absorb primary electrons and compromise energy signal reconstruction through a process called attachment [72, 73]. To address this, the NEWS-G gas handling system includes a gas purifier (or getter) to remove these impurities. Unfortunately, the getter also releases significant amounts of radon, with its daughter elements depositing on the inner surface of the SPC and causing low-energy background events in the region of interest for dark matter searches [67]. Traditional methods like active detector shielding and fiducialization cannot fully reject them.

For our study, we evaluate radon removal performance of silver-zeolite, specifically Ag-ETS-10 [74, 75], compared to the commonly used coconut shell granular activated charcoal (Silcarbon), both tested at room temperature. The rate of radon and its daughter emitters are monitored using a small-scale SPC detector filled with an argon/methane mixture, integrated within a closed-loop circulation system. We show that, at room temperature, the silver-zeolite significantly outperforms activated charcoal by three orders of magnitude in radon capture, with near-complete removal of radon from the system.

Our work considerably extends previous studies on radon trapping with silver-zeolite Ag-ETS-10. The efficacy of various silver-exchanged zeolites has been demonstrated at room temperature in the important works [76–81], with silver-zeolite Ag-ETS-10 consistently emerging as one of the most promising adsorbents for radon mitigation [77, 78]. These earlier studies on Ag-ETS-10 have been conducted with open-loop systems using gases such

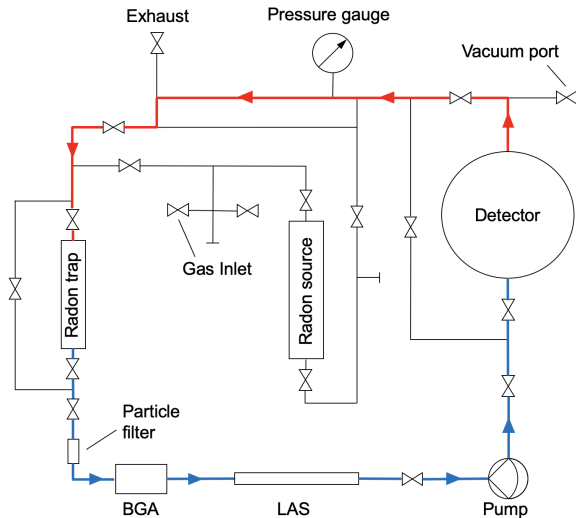


FIG. 1. Closed-loop circulation system for the radon removal campaigns, made of stainless steel fittings, valves and tubing. The setup includes a radon source to diffuse radon into the SPC detector. The gas from the detector (red) circulates through the trap, where radon is adsorbed. The purified gas (blue) is pumped back to the detector, passing through a particle filter, a binary gas analyzer (BGA), and a custom-made laser absorption spectroscopy system (LAS) [76, 84].

as nitrogen, air, or argon and employed a variety of detection methods, including the RadonEye detector and the alphaGUARD monitor. While those detectors are efficient for radon measurement, our work constitutes the first in-situ application of a silver-zeolite trap implemented in a dark matter direct detection-type experiment using an SPC. SPCs offer better energy resolution and sensitivity [69, 82, 83], with the ability to present our findings near background-free in contrast to other methods. Our unique experimental setup shows how the performance of silver-zeolite Ag-ETS-10 traps for radon removal would be in dark matter detectors like NEWS-G and other rare event searches experiments, providing a distinct advantage over other configurations.

Experimental setup—We monitor the event detection rate in a 30 cm diameter stainless steel SPC filled with 500 mbar of a 97% argon and 3% methane mixture. The detector is equipped with a two-mm diameter spherical anode at its center, biased to a positive HV of 1180 V via an insulated HV wire going through the grounded support rod. The operating conditions are selected to contain the track lengths of alpha particles (^{210}Po (8.62 cm), ^{222}Rn (9.09 cm), ^{218}Po (10.3 cm), ^{214}Po (15.1 cm), calculated with SRIM [85]) so that these deposit their full kinetic energy in the gas volume with high amplification gain. During each measurement, the SPC is integrated into a closed-loop circulation system consisting of a radon source, a radon trap, and a pump with a flow of 1 L/min, as shown in Fig. 1. Continuous circulation ensures the

retention of radon in the trap until disintegration, while the purified gas is recirculated back into the detector.

The radon source (Pylon 1025) uses dry ^{226}Ra to produce a calibrated quantity of ^{222}Rn , with an equilibrium activity of 0.93 kBq and a continuous rate of 117.49 mBq. The radon trap consists of a custom 20 cm long stainless steel 1/2-inch tube, filled with 10 g of adsorbent material (silver-zeolite or activated charcoal) and capped at both ends with multi-purpose fiberglass. In addition, a particle filter (60 μm pore size) is installed after the trap to prevent any granules of the adsorbent material from entering sensitive equipment within the circulation system. A binary gas analyzer (BGA) and a custom-made laser absorption spectroscopy system (LAS) are included to monitor the methane concentration in the gas during measurements [76, 84].

Before each measurement, the trap undergoes thermal regeneration at 160°C within the closed-loop system. This process involves flushing with nitrogen gas via the gas inlet to the exhaust, followed by evacuation with a vacuum pump and isolation of the trap [86]. This regeneration, also known as activation, removes any adsorbed gases and contaminants. To further minimize contaminants in the gas loop, the entire system is evacuated to approximately 10^{-7} Torr, except the circulation pump, which cannot achieve a vacuum lower than 10^{-3} Torr. Finally, the gas mixture is injected, filling the system to a pressure of 500 mbar.

Experimental procedure—We conduct three experimental campaigns to test the efficacy of the radon trap at room temperature and demonstrate reproducibility: two with silver-zeolite (campaigns 1 and 2) and one using activated charcoal (campaign 3). To ensure consistency across the campaigns, we organize the data collection into four phases (see Fig. 2): (I) Background: initially, we perform at least a 24-hour background run to determine the minimal sensitivity of the detector; (II) Radon diffusion: radon is injected by diffusion exclusively into the detector for a day until the latter reaches a raw rate of ~ 75 Hz. Once this rate is achieved, we close the radon source and isolate the detector. Continuing diffusion of radon from the gas system eventually raises the rate to ~ 100 Hz. During this period, the rest of the system remains closed and there is no circulation; (III) Radon decay: we monitor the radon decay rate for approximately two days, while the rest of the system remains closed and there is no circulation; (IV) Trap open: the closed-loop system, including the trap, is opened to the detector and the pump is used to circulate the gas, as shown in Fig. 1. Radon is removed at this step.

Data analysis—To interpret the data and assess the experimental results, we apply one of two distinct cuts to the data. The first is a quality cut to specifically remove events from atmospheric muons, which deposit tens of keV in the detector, as well as electronic noise events. The result of applying this cut in all phases of the three

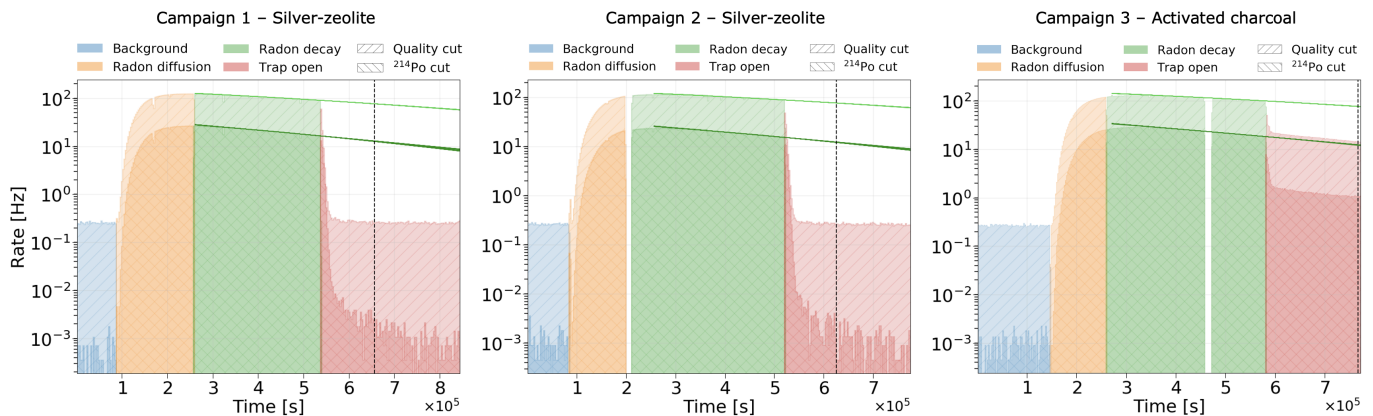


FIG. 2. Measured rate with either quality or ^{214}Po cut applied during the three radon campaigns, with the trap filled with either silver-zeolite or activated charcoal, at room temperature. The blue distribution corresponds to the background run (phase I), orange is the radon diffusion in the SPC (phase II), green is the radon decay (phase III), and red is the events recorded when the radon trap is open (phase IV). The light and dark green curves (with either quality cut or ^{214}Po cut applied, respectively) are the fitted/extrapolated decay rates for each campaign, depicting many random Markov Chain Monte Carlo (MCMC) samples. The vertical dashed line defines the reference time where the expected rate with quality cut is equal to 76.5 Hz. Note that there are some visible gaps in the data (campaigns 2 and 3) due to brief pauses in data collection.

campaigns is shown in Fig. 2. The constant background observed in phase I comes predominantly from the alpha decay of ^{210}Po (5.3 MeV [87]), originating from the stainless-steel inner surface of the SPC detector. It serves as a stable and constant low-rate calibration source for this analysis [86].

The second is the ^{214}Po cut to select only ^{214}Po events. When the radon is injected in phases II and III, the amplitude distribution exhibits different peaks corresponding to ^{222}Rn (5.5 MeV [40]) and the daughter isotopes ^{218}Po (6.0 MeV [88]) and ^{214}Po (7.7 MeV [89]), proportional to the energy of each alpha emitter (see Fig. S1 of [86]). This series of amplitude peaks is used to define a more strict selection of only full energy deposition ^{214}Po events, based on the amplitude minima between the ^{214}Po and ^{218}Po peaks. However, since no ^{214}Po peak features appear in phase I for all campaigns and in phase IV for campaigns 1 and 2, the ^{214}Po cuts in these phases are derived from the ^{210}Po peak and scaled assuming a linear energy response [86]. As shown in Fig. 2, the selection of only ^{214}Po events significantly improves our signal-to-background ratio and allows us to assess our results as near background-free in later analysis.

The expected ^{222}Rn decay rate over time without the intervention of the trap, with either the quality or ^{214}Po cut applied, is determined using the phase III data of each campaign. High event rates (~ 100 Hz) in the SPC cause pileup and dead-time losses of alpha events [90]. To infer the true radon rate from the measured rate in spite of these factors, a Monte Carlo (MC) simulation is designed to emulate the decay process and include expected pileup and dead-time effects [86]. This model is fit to the data using a Markov Chain Monte Carlo (MCMC) [91], jointly incorporating the observed rate in phase III with either

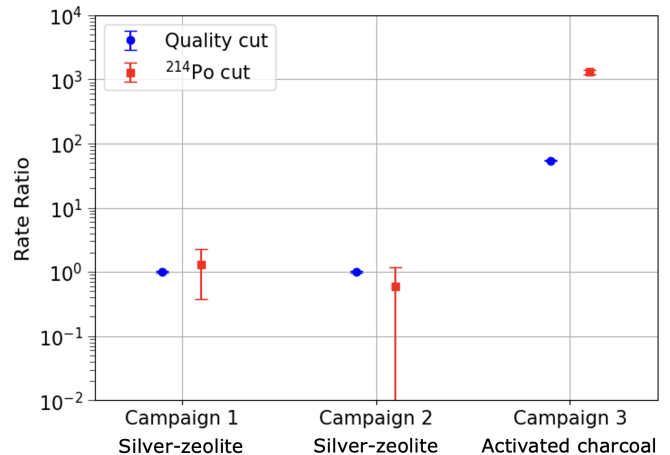


FIG. 3. Ratio between the rate in phase IV (trap open) at the reference time and the rate in phase I (background run) for each campaign with the trap filled with silver-zeolite (campaigns 1 and 2) and activated charcoal (campaign 3). The blue circle and red square represent the rate ratio obtained with either quality cut or ^{214}Po cut, respectively. Complete radon removal correspond to a rate ratio of 1.

the quality or ^{214}Po cut applied. The resulting fit of the observed event rates with each cut applied is shown in Fig. 2, including extrapolations to phase IV for each campaign to show the expected decay rates without the intervention of the radon trap.

Rate comparison—Figure 2 clearly demonstrates that campaigns 1 and 2, which utilize the silver-zeolite trap, outperform campaign 3 using activated charcoal in terms of radon and ^{214}Po event reduction. In particular, in campaigns 1 and 2, the rates in phase IV drop signifi-

cantly before stabilizing. In contrast, the rate remains higher in phase IV of campaign 3, with an exponential decay indicating the presence of radon remaining in the detector.

As an initial assessment of the trap performance, we compare the rates obtained in phases I and IV with either quality or ^{214}Po cut throughout the three campaigns. The rate in phase I for all campaigns is approximately constant, and is fitted with a constant function. To compare this rate with the rate in phase IV after the trap is opened, we define the following reference time. We extrapolate the expected rate from phase III (without trap) with quality cut to later times and determine the reference time where the extrapolation reaches 76.5 Hz (dashed vertical lines in Fig. 2). This procedure is applied in all three campaigns to determine the rates in phases I and IV, see Table S1 of [86]. From this, we calculate the rate ratio between phase IV and phase I with either the quality or ^{214}Po cut, as shown in Fig. 3.

Campaigns 1 and 2, using the silver-zeolite trap, consistently achieve near complete radon removal, whereas the radon levels in the activated charcoal campaign 3 are two to three orders of magnitude higher. As expected, the rate ratio obtained with the ^{214}Po cut is typically larger, but more affected by statistical fluctuations due to the small rate of events in the background measurement of phase I.

Trap performance—To further quantify the performance of the trap, we calculate the radon reduction ratio R (or R-value) from phase IV, defined as

$$R(t) = \frac{R_{\text{exp}}(t)}{R_{\text{obs}}(t)}. \quad (1)$$

Here, $R_{\text{exp}}(t)$ is the expected rate obtained from the extrapolated rate trend and $R_{\text{obs}}(t)$ is the observed rate from the experimental data after the trap is opened. The R-value for each time bin in phase IV is determined by optimizing (with a Nelder-Mead algorithm [92, 93]) a Poisson likelihood comparing the observed count rate with the expected count rate scaled by $R(t)^{-1}$ [86]. The Feldman-Cousins method is applied to determine the 90% confidence level (CL) uncertainty bands for $R(t)^{-1}$ [94]. A rolling-average smoothing over 15 time bins is applied to the best-fit $R(t)^{-1}$ and the 90% CL intervals to mitigate statistical fluctuations in the post-trap data. This process is repeated with many MCMC samples for the extrapolated rate trend model, and the resulting median value of the best-fit $R(t)^{-1}$ and the 90% CL interval is taken in each time bin.

Given the average track length of ^{214}Po events (15.1 cm in the relevant gas conditions [85]) relative to the 30 cm diameter of the SPC, there is the possibility that some events may not deposit all their energy within the detector volume. Further, some fraction of ^{214}Po isotopes are expected to settle on the inner surface of the detector before decaying, increasing the fraction of events that

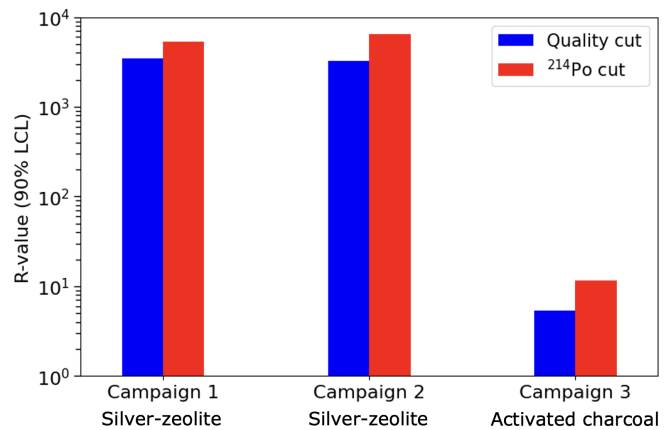


FIG. 4. R-values at 90% lower confidence limit (LCL), obtained at the reference time, with the trap filled with silver-zeolite (campaigns 1 and 2) and activated charcoal (campaign 3). The blue and red bars represent the R-values obtained with either quality cut or ^{214}Po cut (with 50% reduced signal efficiency), respectively.

will not deposit their full energy in the SPC gas. This could result in an underestimation of the actual rate of ^{214}Po . Consequently, the expected and observed ^{214}Po event rates in phase IV are both conservatively reduced by 50% in the calculation of $R(t)^{-1}$.

To quantitatively compare the R-value across all campaigns, we extract the 90% lower confidence limit (LCL) of R at the reference time (see Fig. S3 in [86]). The results are presented in Fig. 4 with the quality cut or the ^{214}Po cut (with 50% reduced signal efficiency) applied. The corresponding values are reported in Table S2 of [86]. In campaigns utilizing silver-zeolite (campaigns 1 and 2), the 90% LCL R-values range from 3.2×10^3 to 6.4×10^3 , which is three orders of magnitude higher than those found in campaign 3, using activated charcoal, where R-values range from 5.3 to 11.6. Moreover, campaigns 1 and 2 demonstrate consistent performance of silver-zeolite, as evidenced by their similar results. As anticipated, R-values derived with the ^{214}Po cut applied are generally higher than those with the quality cut, due to a higher signal-to-background ratio.

Conclusion and outlook—A comparison of the silver-zeolite Ag-ETS-10 and activated charcoal campaigns reveals several critical insights. First, the silver-zeolite trap demonstrates significantly higher efficiency in radon removal, with R-values three orders of magnitude greater than those observed with the activated charcoal trap. Additionally, the rate ratio, which compares event rates after the trap is opened to those before radon diffusion, approaches 1 for the silver-zeolite campaigns, demonstrating near-complete radon removal from the system. In contrast, the activated charcoal campaign exhibits residual radon levels in the rate ratio that are two to three orders of magnitude higher. Finally, in all measurements,

the silver-zeolite campaigns show consistent performance, as evidenced by similar results across both campaigns, confirming reliable and reproducible outcomes.

In this Letter, we demonstrated that silver-zeolite Ag-ETS-10 exhibits superior radon removal efficiency at room temperature compared to activated charcoal, which is commonly used at cryogenic temperatures in rare event search experiments. Our findings highlight the potential of silver-zeolite for developing ambient-temperature radon reduction systems. This advancement is particularly important for underground laboratories, where elevated radon levels compromise the ultra-low background environments required for dark matter and neutrino physics experiments [95, 96]. Integrating silver-zeolite filters into ventilation systems and clean rooms can substantially reduce radon concentrations and enhance the supporting capabilities of these facilities [97, 98]. Moreover, eliminating the need for cryogenic cooling offers significant operational advantages by simplifying system design and reducing the overall complexity of radon reduction systems for future ton-scale detectors. Since our experimental campaigns with silver-zeolite Ag-ETS-10 have been conducted with an actual dark matter-type detector, they serve as a proof of principle for its application in current and future rare event searches.

Acknowledgments—This work was supported by the Canada First Research Excellence Fund through the Arthur B. McDonald Canadian Astroparticle Physics Research Institute and through the University of Alberta startup fund UOFAB Startup Piro. M.-C. P. also acknowledges funding from the Natural Sciences and Engineering Research Council of Canada (NSERC) Subatomic Physics Discovery Grant (project) No. SAPPJ-2024-00025, from which P. G. and Y. D. were further supported. The work of D. D. and C. G. was also supported by the NSERC Graduate Scholarships Doctoral and Master programs, respectively. We are grateful for the support of Compute Ontario [99], the BC DRI Group, and the Digital Research Alliance of Canada [100] required to carry out the simulation needed for this Letter. We thank Hervé Le Provost (IRFU-CEA/Saclay) for his software development work in our data acquisition system. We also thank the NEWS-G collaboration for their technical support of the experimental setup provided for this work and the review of this Letter. We also gratefully thank Daniel Kuznicki for assisting with the silver-zeolite Ag-ETS-10 sample obtained from Extraordinary Adsorbents Inc. of Edmonton, Alberta [74].

* Contact author: ddurnfor@ualberta.ca

† Contact author: ydeng6@ualberta.ca

‡ now at Queen’s University, Ontario, Canada.

§ Contact author: mariucci@ualberta.ca

- [1] E. O’Dwyer, *Radon Background Reduction in DEAP-1 and DEAP-3600*, Master’s thesis, Queen’s University (2011).
- [2] T. Pollmann, *Alpha backgrounds in the DEAP Dark Matter search experiment*, Ph.D. thesis, Queen’s University (2012).
- [3] M. Agostini *et al.* (GERDA), The background in the $0\nu\beta\beta$ experiment GERDA, *Eur. Phys. J. C* **74**, 2764 (2014).
- [4] P. A. Amaudruz *et al.*, Radon backgrounds in the DEAP-1 liquid argon based Dark Matter detector, *Astropart. Phys.* **62**, 178 (2015).
- [5] Y. Nakano *et al.*, Measurement of Radon Concentration in Super-Kamiokande’s Buffer Gas, *Nucl. Instrum. Meth. A* **867**, 108 (2017).
- [6] E. H. Miller *et al.*, Constraining Radon Backgrounds in LZ, *AIP Conf. Proc.* **1921**, 050003 (2018).
- [7] G. Benato *et al.*, Radon mitigation during the installation of the CUORE $0\nu\beta\beta$ decay detector, *JINST* **13** (01), P01010.
- [8] N. Rupp, Radon background in liquid xenon detectors, *JINST* **13** (02), C02001.
- [9] J. Street *et al.*, Radon Mitigation for the SuperCDMS SNOLAB Dark Matter Experiment, *AIP Conf. Proc.* **1921**, 050002 (2018).
- [10] X. Quintana, *Radon measurement for neutrinoless double beta decay*, Master’s thesis, The University of New Mexico Albuquerque (2018).
- [11] A. E. Monte, *Alpha Radiation Studies and Related Backgrounds in the DarkSide-50 Detector*, Ph.D. thesis, Massachusetts U., Amherst (2018).
- [12] P. Novella *et al.* (NEXT), Measurement of radon-induced backgrounds in the NEXT double beta decay experiment, *JHEP* **10**, 112.
- [13] A. H. Abdelhameed *et al.* (CRESST), Geant4-based electromagnetic background model for the CRESST dark matter experiment, *Eur. Phys. J. C* **79**, 881 (2019), [Erratum: *Eur.Phys.J.C* 79, 987 (2019)].
- [14] B. Lehnert (DEAP-3600), Backgrounds in the DEAP-3600 Dark Matter Experiment, *J. Phys. Conf. Ser.* **1342**, 012072 (2020).
- [15] Y. P. Zhang *et al.* (JUNO), Study of the radon removal and detection for JUNO, *J. Phys. Conf. Ser.* **1468**, 012193 (2020).
- [16] D. S. Akerib *et al.* (LZ), The LUX-ZEPLIN (LZ) radioactivity and cleanliness control programs, *Eur. Phys. J. C* **80**, 1044 (2020), [Erratum: *Eur.Phys.J.C* 82, 221 (2022)].
- [17] M. Agostini *et al.* (Borexino), Search for low-energy neutrinos from astrophysical sources with Borexino, *Astropart. Phys.* **125**, 102509 (2021).
- [18] G. Adhikari *et al.* (nEXO), nEXO: neutrinoless double beta decay search beyond 10^{28} year half-life sensitivity, *J. Phys. G* **49**, 015104 (2022).
- [19] A. Aguilar-Arevalo *et al.* (DAMIC), Characterization of the background spectrum in DAMIC at SNOLAB, *Phys. Rev. D* **105**, 062003 (2022).
- [20] E. Aprile *et al.* (XENON), Material radiopurity control in the XENONnT experiment, *Eur. Phys. J. C* **82**, 599 (2022).
- [21] S. M. Hussain, *Evaluating ^{238}U External Background for SNO+ Experiment using Radon Assays and ^{214}Bi Analysis*, Master’s thesis, Laurentian University (2022).
- [22] M. Arthurs, *Radon Reduction and the First Science Re-*

- sults of the LZ Experiment*, Ph.D. thesis, University of Michigan (2022).
- [23] Z. Qian *et al.* (PandaX-4T), Low radioactive material screening and background control for the PandaX-4T experiment, *JHEP* **06**, 147.
- [24] C. Ha *et al.*, Radon concentration variations at the Yangyang underground laboratory, *Front. in Phys.* **10**, 1030024 (2022).
- [25] A. Allega *et al.* (SNO+), Evidence of Antineutrinos from Distant Reactors using Pure Water at SNO+, *Phys. Rev. Lett.* **130**, 091801 (2023).
- [26] J. Street, *Reduction of Radon-daughter Backgrounds for the Super Cryogenic Dark Matter Search Experiment*, Ph.D. thesis, South Dakota School of Mines and Technology Rapid City (2023).
- [27] C. Augier *et al.* (CUPID), The background model of the CUPID-Mo $0\nu\beta\beta$ experiment, *Eur. Phys. J. C* **83**, 675 (2023).
- [28] J. Aalbers *et al.* (LZ), Background determination for the LUX-ZEPLIN dark matter experiment, *Phys. Rev. D* **108**, 012010 (2023).
- [29] J. Aalbers *et al.* (LZ), First Dark Matter Search Results from the LUX-ZEPLIN (LZ) Experiment, *Phys. Rev. Lett.* **131**, 041002 (2023).
- [30] N. I. Chott *et al.* (LZ), Radon emanation techniques and measurements for LZ, *AIP Conf. Proc.* **2908**, 080004 (2023).
- [31] V. Veeraraghavan *et al.*, Simulation studies on backgrounds in nEXO from radon-daughter plate-out, *AIP Conf. Proc.* **2908**, 050001 (2023).
- [32] P. Abratenko *et al.* (MicroBooNE), Measurement of ambient radon progeny decay rates and energy spectra in liquid argon using the MicroBooNE detector, *Phys. Rev. D* **109**, 052007 (2024).
- [33] K. M. Seo *et al.*, Radon concentration measurement with a high-sensitivity radon detector at the Yemilab, *JINST* **19** (05), P05074.
- [34] E. Aprile *et al.* (XENON), Offline tagging of radon-induced backgrounds in XENON1T and applicability to other liquid xenon time projection chambers, *Phys. Rev. D* **110**, 012011 (2024).
- [35] X. Cui *et al.*, Radon removal commissioning of the PandaX-4T cryogenic distillation system, *JINST* **19** (07), P07010.
- [36] S. Miller-Chikowski, *Studies on Radioactive Background Mitigation for the PICO-500 Dark Matter Search Experiment*, Master's thesis, University of Alberta (2024).
- [37] J. Aalbers *et al.* (XLZD), The XLZD Design Book: Towards the Next-Generation Liquid Xenon Observatory for Dark Matter and Neutrino Physics, (2024), [arXiv:2410.17137 \[hep-ex\]](https://arxiv.org/abs/2410.17137).
- [38] J. Aalbers *et al.* (XLZD), Neutrinoless Double Beta Decay Sensitivity of the XLZD Rare Event Observatory, (2024), [arXiv:2410.19016 \[physics.ins-det\]](https://arxiv.org/abs/2410.19016).
- [39] A. Lahaie *et al.* (SuperNEMO), Study of Radon background in the SuperNEMO detector, *PoS ICHEP2024*, 199 (2025).
- [40] B. Singh *et al.*, Nuclear data sheets for A=218, *Nucl. Data Sheets* **160**, 405 (2019).
- [41] K. Abe *et al.* (XMASS), Identification of ^{210}Pb and ^{210}Po in the bulk of copper samples with a low-background alpha particle counter, *Nucl. Instrum. Meth. A* **884**, 157 (2018).
- [42] R. Bunker *et al.*, Evaluation and mitigation of trace ^{210}Pb contamination on copper surfaces, *Nucl. Instrum. Meth. A* **967**, 163870 (2020).
- [43] L. Balogh *et al.* (NEWS-G), Copper electroplating for background suppression in the NEWS-G experiment, *Nucl. Instrum. Meth. A* **988**, 164844 (2021).
- [44] C. Vivo-Vilches *et al.*, ^{210}Pb measurements at the André E. Lalonde AMS Laboratory: Potential for the radioassay of materials used in rare event search detectors, *Nucl. Instrum. Meth. B* **511**, 51 (2022).
- [45] M. Murra *et al.*, Design, construction and commissioning of a high-flow radon removal system for XENONnT, *Eur. Phys. J. C* **82**, 1104 (2022).
- [46] K. Abe *et al.*, Radon removal from gaseous xenon with activated charcoal, *Nucl. Instrum. Meth. A* **661**, 50 (2012).
- [47] Y. Y. Chen *et al.*, A study on the radon removal performance of low background activated carbon, *JINST* **17** (02), P02003.
- [48] P. Abratenko *et al.* (MicroBooNE), Observation of radon mitigation in MicroBooNE by a liquid argon filtration system, *JINST* **17** (11), P11022.
- [49] C. Li *et al.*, Study on the radon adsorption capability of low-background activated carbon, *J. Radioanal. Nucl. Chem.* **333**, 337 (2024).
- [50] N. Fatemighomi *et al.*, Measurement of low ^{222}Rn concentration in N_2 using an activated charcoal trap, *Nucl. Instrum. Meth. A* **1076**, 170422 (2025).
- [51] E. Aprile *et al.* (XENON), Online ^{222}Rn removal by cryogenic distillation in the XENON100 experiment, *Eur. Phys. J. C* **77**, 358 (2017).
- [52] C. E. Aalseth *et al.* (DarkSide-20k), DarkSide-20k: A 20 tonne two-phase LAr TPC for direct dark matter detection at LNGS, *Eur. Phys. J. Plus* **133**, 131 (2018).
- [53] S. E. Vahsen *et al.*, CYGNUS: Feasibility of a nuclear recoil observatory with directional sensitivity to dark matter and neutrinos, (2020), [arXiv:2008.12587 \[physics.ins-det\]](https://arxiv.org/abs/2008.12587).
- [54] A. S. García-Viltres *et al.* (PICO), PICO-500: A tonne scale bubble chamber for the search of dark matter, *Nuovo Cim. C* **45**, 7 (2021).
- [55] V. Albanese *et al.* (SNO+), The SNO+ experiment, *JINST* **16** (08), P08059.
- [56] A. Abusleme *et al.* (JUNO), JUNO physics and detector, *Prog. Part. Nucl. Phys.* **123**, 103927 (2022).
- [57] A. Armato *et al.* (CUPID), Toward CUPID-1T, (2022), [arXiv:2203.08386 \[nucl-ex\]](https://arxiv.org/abs/2203.08386).
- [58] S. Abe *et al.* (KamLAND-Zen), Search for the Majorana Nature of Neutrinos in the Inverted Mass Ordering Region with KamLAND-Zen, *Phys. Rev. Lett.* **130**, 051801 (2023).
- [59] L. Balogh *et al.* (NEWS-G), Exploring light dark matter with the DarkSPHERE spherical proportional counter electroformed underground at the Boulby Underground Laboratory, *Phys. Rev. D* **108**, 112006 (2023).
- [60] P. Novella (NEXT), NEXT-White results and roadmap towards a ton-scale detector, *J. Phys. Conf. Ser.* **2502**, 012005 (2023).
- [61] K. Abe *et al.* (Hyper-Kamiokande), Hyper-Kamiokande construction status and prospects, *Front. in Phys.* **12**, 1378254 (2024).
- [62] A. B. McDonald, Dark matter detection with liquid argon, *Nucl. Phys. B* **1003**, 116436 (2024).
- [63] P. Agnes *et al.* (GADMC), The underground argon project: procurement and purification of argon for

- dark matter searches and beyond, *Front. in Phys.* **12**, 1387069 (2024).
- [64] A. Abdurkerim *et al.* (PandaX-4T), PandaX-xT—A deep underground multi-ten-tonne liquid xenon observatory, *Sci. China Phys. Mech. Astron.* **68**, 221011 (2025).
- [65] A. Abed Abud *et al.* (DUNE), DUNE Phase II: scientific opportunities, detector concepts, technological solutions, *JINST* **19** (12), P12005.
- [66] S. Calgario (LEGEND), The Ton-Scale Search for Neutrinoless Double-Beta Decay in Germanium with LEGEND-1000, *PoS ICHEP2024*, 193 (2025).
- [67] L. Balogh *et al.* (NEWS-G), The NEWS-G detector at SNOLAB, *JINST* **18** (02), T02005.
- [68] M. M. Arora *et al.* (NEWS-G), Search for Light Dark Matter with NEWS-G at the Laboratoire Souterrain de Modane Using a Methane Target, *Phys. Rev. Lett.* **134**, 141002 (2025).
- [69] A. Brossard (NEWS-G), Spherical proportional counters; development, improvement and understanding, *Nucl. Instrum. Meth. A* **936**, 412 (2019).
- [70] A. Dastgheibi-Fard and G. Gerbier (NEWS-G), Development of Spherical Proportional Counter for light WIMP search within NEWS-G collaboration, *Nucl. Instrum. Meth. A* **958**, 162390 (2020).
- [71] Q. Arnaud *et al.* (NEWS-G), Precision laser-based measurements of the single electron response of spherical proportional counters for the NEWS-G light dark matter search experiment, *Phys. Rev. D* **99**, 102003 (2019).
- [72] Q. Arnaud *et al.* (NEWS-G), First results from the NEWS-G direct dark matter search experiment at the LSM, *Astropart. Phys.* **97**, 54 (2018).
- [73] A. Brossard, *Optimization of spherical proportional counter backgrounds and response for low mass dark matter search*, Ph.D. thesis, Queen's University (2020).
- [74] See <https://extraordinaryadsorbents.com>.
- [75] S. Kuznicki *et al.*, Xenon adsorption on modified ets-10, *J. Phys. Chem. C* **111**, 1560–1562 (2007).
- [76] P. O'Brien, *Optimization of Processing Parameters and Development of a Radon Trapping System for the NEWS-G Dark Matter Detector*, Master's thesis, University of Alberta (2021).
- [77] S. Heinitz *et al.*, Adsorption of radon on silver exchanged zeolites at ambient temperatures, *Scientific Reports* **13**, 6811 (2023).
- [78] O. Veselska *et al.*, Exploring the potential use of silver-exchanged zeolites for adsorption of radon traces in low background experiments, *Progress of Theoretical and Experimental Physics* **2024**, 023C01 (2023).
- [79] H. Ogawa *et al.*, Measurement of radon emanation and impurity adsorption from argon gas using ultralow radioactive zeolite, *JINST* **19** (02), P02004.
- [80] T. Sone *et al.*, Study of Radon Removal Performance of Silver-Ion Exchanged Zeolite from Air for Underground Experiments, *PTEP* **2025**, 013H01 (2025).
- [81] H. Ogawa *et al.*, Removal of radioactive noble gas radon from air by ag-zeolite, *Progress of Theoretical and Experimental Physics* **2025**, 023H04 (2025).
- [82] I. Giomataris *et al.*, A Novel large-volume Spherical Detector with Proportional Amplification read-out, *JINST* **3**, P09007.
- [83] I. Giomataris *et al.*, Neutron spectroscopy with a high-pressure nitrogen-filled spherical proportional counter, *Nucl. Instrum. Meth. A* **1049**, 168124 (2023).
- [84] C. Garrah, *On Advances in LAS Instrumentation and Fiducial Volume Simulations of the S140 Detector for the NEWS-G Dark Matter Search Experiment*, Master's thesis, University of Alberta (2023).
- [85] J. F. Ziegler *et al.*, SRIM – the stopping and range of ions in matter (2010), *Nucl. Instrum. and Methods Phys. Res. Sect. B* **268**, 1818 (2010).
- [86] See Supplemental Material for regeneration process, details on analysis methods for quality and ^{214}Po cuts, expected rates from MC simulation and MCMC fit, rates in phases I and IV, R-values over time and values at the reference time, which includes Refs. [101–108].
- [87] F. G. Kondev, Nuclear data sheets for A=206, *Nucl. Data Sheets* **109**, 1527 (2008).
- [88] S. Zhu and others., Nuclear data sheets for A=214, *Nucl. Data Sheets* **175**, 1 (2021).
- [89] M. S. Basunia, Nuclear data sheets for A=210, *Nucl. Data Sheets* **121**, 561 (2014).
- [90] D. Durnford, *The search for low mass dark matter with the NEWS-G and SBC experiments*, Ph.D. thesis, University of Alberta (2024).
- [91] D. Foreman-Mackey *et al.*, emcee: The MCMC Hammer, *Publ. Astron. Soc. Pac.* **125**, 306 (2013).
- [92] P. Virtanen *et al.*, SciPy 1.0—Fundamental Algorithms for Scientific Computing in Python, *Nature Meth.* **17**, 261 (2020).
- [93] F. Gao and L. Han, Implementing the Nelder-Mead simplex algorithm with adaptive parameters, *Comput. Optim. Appl.* **51**, 259 (2012).
- [94] G. J. Feldman and R. D. Cousins, A Unified approach to the classical statistical analysis of small signals, *Phys. Rev. D* **57**, 3873 (1998).
- [95] C. Cui *et al.*, Environmental radon control in the 700 m underground laboratory at JUNO, *Eur. Phys. J. C* **84**, 120 (2024).
- [96] P. Huang *et al.*, Impact of environmental factors on atmospheric radon variations at China Jinping Underground Laboratory, *Scientific Reports* **14**, 31402 (2024).
- [97] A. Kamaha *et al.*, Supporting Capabilities For Underground Facilities, (2022), [arXiv:2209.07588](https://arxiv.org/abs/2209.07588) [hep-ex].
- [98] L. Baudis *et al.*, Snowmass 2021 Underground Facilities & Infrastructure Frontier Report, (2022), [arXiv:2211.13450](https://arxiv.org/abs/2211.13450) [hep-ex].
- [99] See <https://computeontario.ca>.
- [100] See <https://www.alliancecan.ca>.
- [101] B. W. Silverman, in *Density Estimation for Statistics and Data Analysis* (Routledge, 1998) p. 95, 1st ed.
- [102] B. Wang and X. Wang, Bandwidth selection for weighted kernel density estimation, *Elec. J. Stat.* **10.1214/1549578041000000000** (2007).
- [103] H. Shimazaki and S. Shinomoto, Kernel bandwidth optimization in spike rate estimation, *J. Comput. Neurosci.* **29**, 171 (2010).
- [104] M. Thorben and M. Walmsley, *Adaptive Width KDE with Gaussian Kernels* (2022), <https://github.com/mennthor/awkde>.
- [105] B. Efron and R. J. Tibshirani, *An Introduction to the Bootstrap*, 1st ed. (Chapman and Hall/CRC, 1994).
- [106] *SciPy Univariate Spline*.
- [107] J. Goodman and J. Weare, Ensemble samplers with affine invariance, *Comm. Appl. Math. Comput. Sci.* **5**, 65 (2010).
- [108] D. Foreman-Mackey *et al.*, emcee: The MCMC hammer, *Publ. Astron. Soc. Pac.* **125**, 306 (2013).

Supplemental Material

This Supplemental Material provides further technical details regarding the regeneration process of the absorbers, the cuts used in our data analysis, the expected decay rates derived with a Monte Carlo (MC) model and Markov Chain Monte Carlo (MCMC) fit, the rates in phases I and IV obtained throughout the campaigns, and calculation of the R-values.

CONTENTS

S1. Regeneration process	8
S2. Analysis details	8
Quality cut	8
^{214}Po cut	9
Expected decay rates	9
S3. Rates in phases I and IV	10
S4. R-values	11

S1. REGENERATION PROCESS

The regeneration process (or activation) involves flushing the trap with nitrogen for 20 minutes, while heating it to 160°C using a heating tape. The temperature is monitored with a thermocouple attached to the exterior surface of the trap. After flushing, the trap is vacuumed for another 20 minutes while maintaining the temperature at 160°C . Once this process is completed, we stop the heating and maintain the vacuum in the trap until it cools to room temperature. Finally, the valves are closed to isolate the trap from the circulation system. This process is used for both silver-zeolite and activated charcoal.

S2. ANALYSIS DETAILS

In this section, we provide details on the data selection criteria with applied quality cut and ^{214}Po cut, and describe the methodology used to determine the expected decay rates of radon and ^{214}Po .

Quality cut

We apply a quality cut that includes a loose pulse shape discrimination cut to remove non-physical events with characteristically short risetimes [72], as well as requiring pulse amplitudes above 1200 ADU (arbitrary digital units). The latter selection removes most of the background events from atmospheric muons, as well as additional electronic noise events. Some degraded alpha

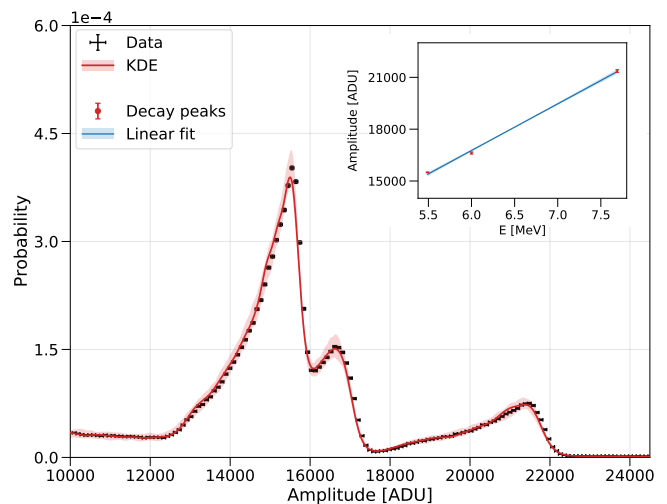


FIG. S1. Amplitude distribution of events for approximately 6 hours of data in phase III recorded by the SPC (black markers). The distribution is modeled with an adaptive-bandwidth Gaussian kernel density estimation [101–104] with bootstrapped [105] statistical uncertainty (red curve and 1σ shaded band). The inset shows the amplitude peak positions corresponding to the maximum energy deposition of three alpha decays versus the corresponding alpha energies (red markers with error bars), with a linear fit (blue curve and shaded band).

events that do not deposit their full kinetic energy also fall below this cut. However, the fraction of affected alpha events remains mostly constant over time, tending to increase slightly as the detector gain decreases. A separate study quantifying the impact of this effect on signal efficiency due to this cut shows a drop of only $\sim 1\%$ over time (see Fig. 3.59 in Ref. [90]).

The remaining constant background in phase I for all campaigns (see Fig. 2 in the main text) comes predominantly from the alpha decay of ^{210}Po (5.3 MeV [87]), originating from radioisotope depositions on the inner surface of the detector material. The SPC, made of stainless steel, does not have particular precautions to prevent ^{210}Po contamination, but can nonetheless serve as a useful low-rate calibration source for this analysis. In phase IV, following the opening of the trap, the rate in campaigns 1 and 2 decreases significantly over several hours, eventually reaching the ^{210}Po alpha background level observed in phase I. For campaign 3, using activated charcoal, the rate remains up to two orders of magnitude higher compared to the rate in phase I and exhibits exponential decay, indicating the continued presence of radon.

In phases II and III, with the injection of radon, the rate increases. By applying the quality cut, we select primarily the full energy alpha decays of ^{222}Rn (5.5 MeV [40]) and its daughter isotopes, ^{218}Po (6.0 MeV [88]) and ^{214}Po (7.7 MeV [89]), which have clear amplitude peaks (above 12,000 ADU) in the recorded data, as shown in

Fig. S1 for phase III. The nominal radon trap analysis described in the main text is performed on the data with only this quality cut applied, incorporating events of all three alpha decay isotopes; as these decays are in secular equilibrium, the proportion of events due to radon itself is approximately constant throughout each measurement campaign. Additionally, high energy beta decay events from the ^{222}Rn decay chain (^{214}Bi in particular [88]) are present in this data selection, but are also in equilibrium with the rest of the decay chain.

To verify the linear energy response of the SPC in this regime, amplitude spectra—such as the one shown in Fig. S1—are characterized with an adaptive-bandwidth Gaussian kernel density estimation [101–104], with statistical uncertainties being estimated using a bootstrapping procedure [105]. The resulting peak amplitudes are well-fit by a linear function of the corresponding alpha decay energies, as shown in the inset of Fig. S1. A peak corresponding to ^{210}Po might be present in this amplitude spectrum, but its rate is more than two orders of magnitude lower than the ^{222}Rn peak with which it overlaps.

^{214}Po cut

In our analysis, we develop a method to select only ^{214}Po events. ^{214}Po decays achieve secular equilibrium with ^{222}Rn due to its short half-life (164 μs [89]) compared to ^{222}Rn and its subsequent daughter isotopes. By selecting only ^{214}Po events, the signal-to-background ratio is significantly improved, as there is no ^{210}Po background in this amplitude regime.

The ^{214}Po cut applied in phases II and III is identified by the time-evolving minima between the ^{218}Po and ^{214}Po peaks (e.g. see Fig. S1), within approximately 6-hour data segments. This method cannot be applied directly to phase I of all campaigns and phase IV of campaigns 1 and 2, since there is no ^{214}Po amplitude peak feature. Instead, during these phases, the ^{210}Po amplitude peak is identified within similar 6-hour data segments, fitted with a linear function over time, and scaled to match the ^{214}Po peak position in phases II/III, assuming energy linearity in this regime. Figure S2 illustrates the evolution of the ^{214}Po amplitude cut across all phases for campaign 1.

Due to the significant amount of radon remaining in phase IV of campaign 3 (see Fig. 2 in the main text), the ^{214}Po amplitude cut is determined using a similar method as in phases II and III. To obtain a time-dependent ^{214}Po amplitude cut for phase IV, the amplitude minima between the ^{218}Po and ^{214}Po peaks are found in approximately 6-hour data segments. The bootstrap resampling [105] is then applied to estimate the statistical uncertainty for each point. These points are then fit with a linear function to define the ^{214}Po amplitude cut for phase IV.

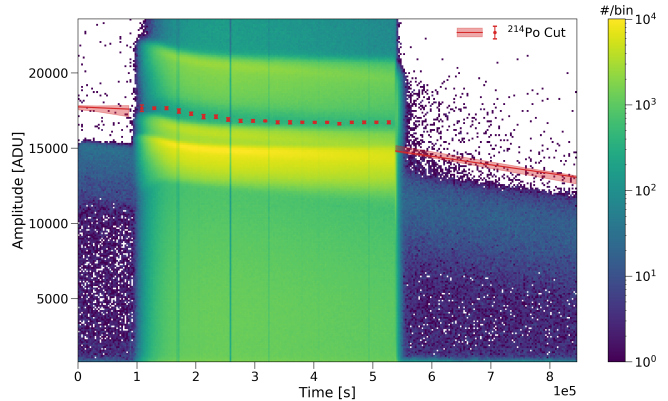


FIG. S2. 2D histogram of the amplitude distribution over time in campaign 1 with the trend of ^{214}Po cut obtained across all phases. In phases II and III, the ^{214}Po cut is defined as the amplitude minima between the ^{218}Po and ^{214}Po peaks in time bins of approximately 6 hours duration, indicated as red markers with statistical error bars. In phases I and IV, a linear fit of the ^{210}Po peak position over time is scaled to match the ^{214}Po cut at the beginning of phase II/end of phase IV, shown as red curves with shaded 1σ uncertainties.

Expected decay rates

Evaluating the performance of the adsorbent requires determining the expected decay rates of radon and its daughters over time without the intervention of the trap. However, operating the SPC at event rates near 100 Hz with a 2 ms event acquisition time window introduces a significant probability of coincidental events, or pileup, and causes dead-time losses due to limitations in the data acquisition (DAQ) system. These effects reduce the observed decay rate compared to the true rate and introduce potential sources of systematic error in subsequent analyzes. It is therefore necessary to infer the true radon rate from the measured rate, accounting for pileup and dead-time losses.

To achieve this, a Monte Carlo (MC) simulation of radon decay is produced for a given radon rate in addition to a given background rate, which includes the expected pileup and dead-time effects to reflect the actual conditions of our experiment. Any simulated decays occurring within 1 ms of each other (half the duration of a single event window) are treated as coincident events (resulting in a single recorded event). Simulated decays occurring within 1 to 2 ms of a preceding pulse are considered as lost due to DAQ deadtime. This approach accounts for the DAQ software centering the maximum amplitude of the triggered event trace within its acquisition time window, ensuring that no two pulses can be more than half an event window apart and still be contained in the event window. High-statistics MCs are produced for true radon rates ranging from approximately 30 Hz to 200 Hz, along with the measured ^{210}Po background rate for each cam-

paign described in the main text. Each MC dataset spans a duration longer than the real data from phase III, covering both phase III and phase IV. The resulting log-scale rate trends—separated into single decay event vs. pileup events—are characterized using univariate splines [106].

The results of the decay rate MCs are incorporated into a joint model for the observed event rate over time, with and without the application of the ^{214}Po cut. The free parameters of the model define: (i) the true radon decay rate from the discrete sets of values for which MCs are produced; (ii) the overall alpha event signal efficiency with the quality cut applied (f_α); (iii) signal efficiency of observed ^{214}Po events with the ^{214}Po cut applied ($f_{\text{Po-214}}$); (iv) the fraction of pileup events in the data without and with the ^{214}Po cut (f_{pileup} and $f_{\text{pileup, Po-214}}$, respectively). Adding the background rates for each data selection (η and $\eta_{\text{Po-214}}$), the expected event rates over time ν , with either the quality or ^{214}Po cut, are given as

$$\begin{aligned} \nu(t) &= f_\alpha \left[10^{y_{\text{Rn-222}}(t)} + 10^{y_{\text{Po-218}}(t)} + 10^{y_{\text{Po-214}}(t)} \right] \\ &+ f_{\text{pileup}} \times 10^{y_{\text{pileup}}(t)} + \eta, \\ \nu_{\text{Po-214}}(t) &= f_{\text{Po-214}} \times 10^{y_{\text{Po-214}}(t)} \\ &+ f_{\text{pileup, Po-214}} \times 10^{y_{\text{pileup}}(t)} + \eta_{\text{Po-214}}, \end{aligned} \quad (\text{S1})$$

where $y_{\text{Rn-222}}(t)$, $y_{\text{Po-218}}(t)$, $y_{\text{Po-214}}(t)$, and $y_{\text{pileup}}(t)$ are the interpolated values from the decay MC splines for the corresponding radon decay chain isotopes and pileup events, respectively.

A joint, binned, Poisson log likelihood function is derived for the event rate over time given this model;

$$\begin{aligned} \log \mathcal{L} &= \sum_i [h_3(i) \log \nu(t_i) - \nu(t_i)] \\ &+ \sum_i [h_3^{\text{Po-214}}(i) \log \nu_{\text{Po-214}}(t_i) - \nu_{\text{Po-214}}(t_i)], \end{aligned} \quad (\text{S2})$$

where $h_3(i)$ and $h_3^{\text{Po-214}}(i)$ are the observed event counts in phase III in time bin i (with central time t_i) with the quality cut and ^{214}Po cut applied, respectively. This model is fit to the data using a Markov Chain Monte Carlo (MCMC). Specifically, the PYTHON package `emcee` is used with the “stretch-move” Metropolis-Hastings algorithm [107, 108], propagating the 100 random walkers for 2×10^5 steps after an initial burn-in phase of 4×10^4 steps. This exceeds the recommendation that the number be at least $50 \times$ the estimated autocorrelation time [108]. The resulting fits (with statistical uncertainty in the form of random MCMC samples) are shown for each campaign in Fig. 2 in the main text.

S3. RATES IN PHASES I AND IV

For the three campaigns, we compare the rates obtained in phases I and IV, with either the quality or ^{214}Po cut. The rate in phase I for all campaigns is approximately constant and is determined by the average count of all time bins in this phase. Similarly, the constant rate in phase IV of campaigns 1 and 2 is calculated starting from the reference time (vertical dashed line in Fig. 2 of the main text). However, in campaign 3, the rate decreases exponentially. To facilitate comparison with campaigns 1 and 2, we also determine the rate in phase IV at the reference time for all campaigns. Table S1 summarizes the rate in phases I and IV with the quality and ^{214}Po cuts, as well as the rate in phase IV for all campaigns, calculated at the reference time.

	Phase I rate (Hz)	Phase IV rate (Hz)
Quality Cut		
Campaign 1	0.252 ± 0.002	$0.254 \pm 0.001^{\text{a}}$ $0.251 \pm 0.009^{\text{b}}$
Campaign 2	0.262 ± 0.002	$0.260 \pm 0.001^{\text{a}}$ $0.262 \pm 0.011^{\text{b}}$
Campaign 3	0.266 ± 0.001	— $14.5 \pm 0.08^{\text{b}}$
^{214}Po cut		
Campaign 1	$(5.36 \pm 0.62) \times 10^{-4}$	$(7.58 \pm 0.66) \times 10^{-4\text{a}}$ $(7.07 \pm 5.00) \times 10^{-4\text{b}}$
Campaign 2	$(7.55 \pm 0.78) \times 10^{-4}$	$(8.63 \pm 0.86) \times 10^{-4\text{a}}$ $(4.50 \pm 4.50) \times 10^{-4\text{b}}$
Campaign 3	$(8.18 \pm 0.67) \times 10^{-4}$	— $1.07 \pm 0.02^{\text{b}}$

^a Rate calculated from constant fit after the reference time.

^b Rate calculated at the reference time.

TABLE S1. Rate in phase I (background) and phase IV (trap open) with either the quality or ^{214}Po cut for all campaigns. The rate in phase IV at the reference time is also included for all campaigns.

The rates in phase I with the quality cut are consistent, although campaigns 2 and 3 exhibit a slightly higher rate. This small increase may be attributed to the buildup of ^{210}Po on the inner surface or volume of the SPC due to consecutive injections of radon over time. Similarly, for the ^{214}Po cut, the rates align closely within the uncertainties with a slight increase. The same trend is observed in phase IV when comparing the rates of campaigns 1 and 2 with the quality and ^{214}Po cuts. Nonetheless, the ratio between the rates in phase IV and phase I for campaigns 1 and 2 approaches 1 (see Fig. 3 in the main text), indicating that the radon rate quickly reduces to pre-injection

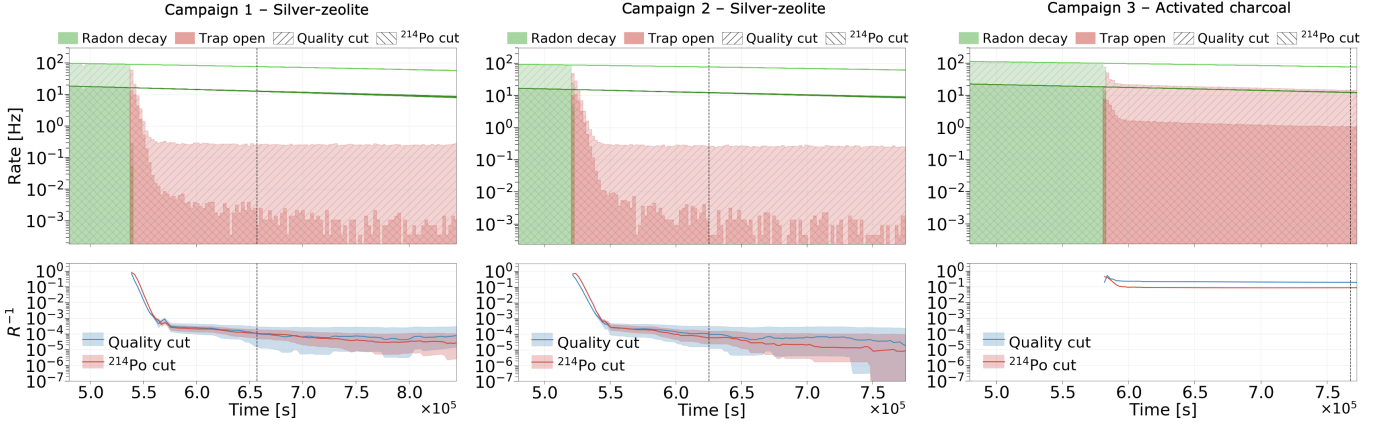


FIG. S3. *Top panel* Expected decay rates with either the quality cut (light green curves) or ^{214}Po cut (dark green curves) applied, derived from modeling of the phase III data from each campaign (green histograms), as well as the phase IV data (red histograms). *Bottom panel* Inverse R-values over time, obtained with the quality cut (red curves) and ^{214}Po cut (50%) applied (blue curves), including their respective 90% confidence level (CL) intervals. The vertical dashed line defines the reference time where the rate with quality cut (light green line) is equal to 76.5 Hz.

levels in campaigns 1 and 2. This also demonstrates that the performance of the radon trap aligns well with the achievable sensitivity of our experimental setup.

S4. R-VALUES

In this section, we describe how the R-value (specifically $R(t)^{-1}$, see Eq. 1 in the main text) is obtained for each measurement campaign. Separate results with and without the ^{214}Po cut are derived by first defining a log likelihood function for the phase IV data of each campaign in each time bin i , scaling the phase III decay rate trend by $R(t_i)^{-1}$ and allowing the background rate η to vary as a nuisance parameter:

$$\log \mathcal{L}_R(i) = h_4(i) \log \nu(t_i) - \nu(t_i) - \frac{1}{2} \left(\frac{\eta - \eta_{\text{obs}}}{\sigma_\eta} \right)^2, \quad (\text{S3})$$

where the latter term is a Gaussian constraint term for the background rate with respect to the observed background rate (from phase I) and its uncertainty (η_{obs} and σ_η , respectively). $h_4(i)$ is the observed event counts in phase IV in time bin i . The expected count rate in the center of each time bin, $\nu(t_i)$, is equal to the expected rate trend from phase III (see Eq. S1) multiplied by $R(t_i)^{-1}$, plus η . For the calculation of $R(t_i)^{-1}$ with ^{214}Po cuts, we conservatively assume a 50% detection efficiency for ^{214}Po events, due to the possibility that many isotopes may have settled on the detector surface and then emit alphas away from the detector volume.

The best-fit value of $R(t_i)^{-1}$ is determined in each time bin with the PYTHON `scipy.optimize.minimize` class,

with a Nelder-Mead method specifically [92, 93], profiling over the background rate. A 90% confidence level (CL) interval is then calculated using the Feldman-Cousins method [94]. To address significant statistical fluctuations in the data count rate over time, a rolling-average algorithm (over 15 time bins) is applied to the best-fit $R(t)^{-1}$ and 90% CL interval. The above procedure is performed 125 times to include statistical uncertainty on the phase III rate model, varying the model parameters with randomly drawn MCMC samples. This yields an ensemble of slightly different best-fit $R(t_i)^{-1}$ and corresponding 90% CL intervals for each time bin, of which we take the median result for each.

The $R(t)^{-1}$, along with the corresponding 90% CL intervals, are shown in the bottom panels of Fig. S3 for each campaign. From these results, we determine the final R-value, $R(t)$, at the reference time, which is denoted by vertical dashed lines in Fig. S3. The derived values and their associated 90% CL intervals for either the quality cut or the ^{214}Po cut (50%) are summarized in Table S2.

	Quality cut	^{214}Po cut (50%)
Campaign 1	9605.64 [3465.66, 67957.1]	9376.55 [5286.86, 19292.9]
Campaign 2	10023.5 [3234.85, 76679.6]	17057.9 [6449.61, 43815.8]
Campaign 3	5.39002 [5.34640, 5.43372]	11.7936 [11.6108, 11.9752]

TABLE S2. R-values with the 90% CL intervals (lower and upper limits) at the reference time with either quality cut or ^{214}Po cut (50%) applied for each campaign. The 90% lower confidence limit (LCL) is reported as the final result of R-value for each campaign and shown in Fig. 4 in the main text.